Tailoring Optical Vortical Dichroism with Stereometamaterials

Shunli Liu, Jincheng Ni, Cong Zhang, Xinghao Wang, Yang Cao, Dawei Wang, Shengyun Ji, Deng Pan, Rui Li, Hao Wu, Chen Xin, Jiawen Li,* Yanlei Hu, Guixin Li, Dong Wu,* and Jiaru Chu

Chiroptical response, investigating the interaction between photonic angular momenta and chiral media, is widely applied in optics and material science. In photonic spin angular momentum (SAM) dimension, tailoring circular dichroism (CD) is realized by varying chiral metamaterials for compact circular polarizers and enantiomer sensing. However, in photonic orbital angular momentum (OAM) dimension, tailorable chiroptical property by artificial metamaterials at a fixed operating wavelength remains elusive. Here, it is proposed and demonstrated that twisted stereometamaterials can yield OAM-dependent tailorable vortical dichroism (VD) ranging from −97% to +98%. Engineering the geometrical parameters and symmetry of the twisted stereometamaterials can flexibly control the spectral characteristics of VD measurements such as sign, magnitude, and position. The twisted stereometamaterials, managing the transmission behaviors of light with various OAM, holds great promise for developing miniaturized components in integrated photonics and chiroptical spectroscopy.

1. Introduction

Chiroptical response is a momentous phenomenon of chiral light-matter interactions, which has been extensively studied in the past and still attracts enormous attention in modern optics.[1–4] One of the most significant chiroptical manifestations is circular dichroism (CD), defined as the differential absorption of left- and right-handed circularly polarized light after passing through chiral media.[5,6] As an intuitive demonstration of optical chiral properties, the CD spectroscopy has been widely used in metamaterial design,[7–9] enantiomer identification,[10,11] and

S. Liu, J. Ni, C. Zhang, X. Wang, Y. Cao, D. Wang, S. Ji, D. Pan, R. Li,
H. Wu, C. Xin, J. Li, Y. Hu, D. Wu, J. Chu
CAS Key Laboratory of Mechanical Behavior and Design of Materials
Department of Precision Machinery and Precision Instrumentation
University of Science and Technology of China
Hefei, Anhui 230027, China
E-mail: jwl@ustc.edu.cn; dongwu@ustc.edu.cn
G. Li
Department of Materials Science and Engineering
Southern University of Science and Technology
Shenzhen 518055, China

The ORCID identification number(s) for the author(s) of this article can be found under https://doi.org/10.1002/lpor.202100518

polarization detection.[12–14] Furthermore, tailoring spectral characteristics of CD has been realized through the judiciously designed chiral plasmonic nanostructures.[15–18] Recently, it was reported that light waves with intrinsic chiral characteristic possess angular momentum. For example, circularly polarized light with helical electric vectors carries spin angular momentum (SAM). In addition, optical vortices with helical wavefronts intrinsically carry orbital angular momentum (OAM), which is determined by the OAM mode index.[19,20] Analogous to the SAM-dependent CD, the optical phenomenon related to photonic OAM is crucial for expanding the dimensions of chiroptical responses.

Distinguished with the polarization-related SAM, the phase-related OAM has great applications in optical wrenches,[21–22] optical holography,[23–25] chiral structure processing,[26–28] and optical communications.[29,30] With the deepening understanding of photonic OAM, it gradually begins to be explored in chiroptical response.[31,32] For example, it has been confirmed that the chirality of incident OAM light can be detected by a dipolar chiral nanostructure.[33] Inversely, the chirality of multiscale chiral structures can be distinguished by the OAM light.[34–35] These phenomena are based on the transmission difference of light with opposite OAM states, which is dubbed vortical dichroism (VD). Essentially different from SAM-contributed CD, the VD reveals the interaction between photonic OAM and chiral media. As an emerging chiroptical response in photonic OAM dimension, it is significant to realize tailorable VD for managing the transmission behaviors of OAM beams in integrated photonics. However, the on-demand VD tailor via designing chiral metamaterials has not yet been realized.
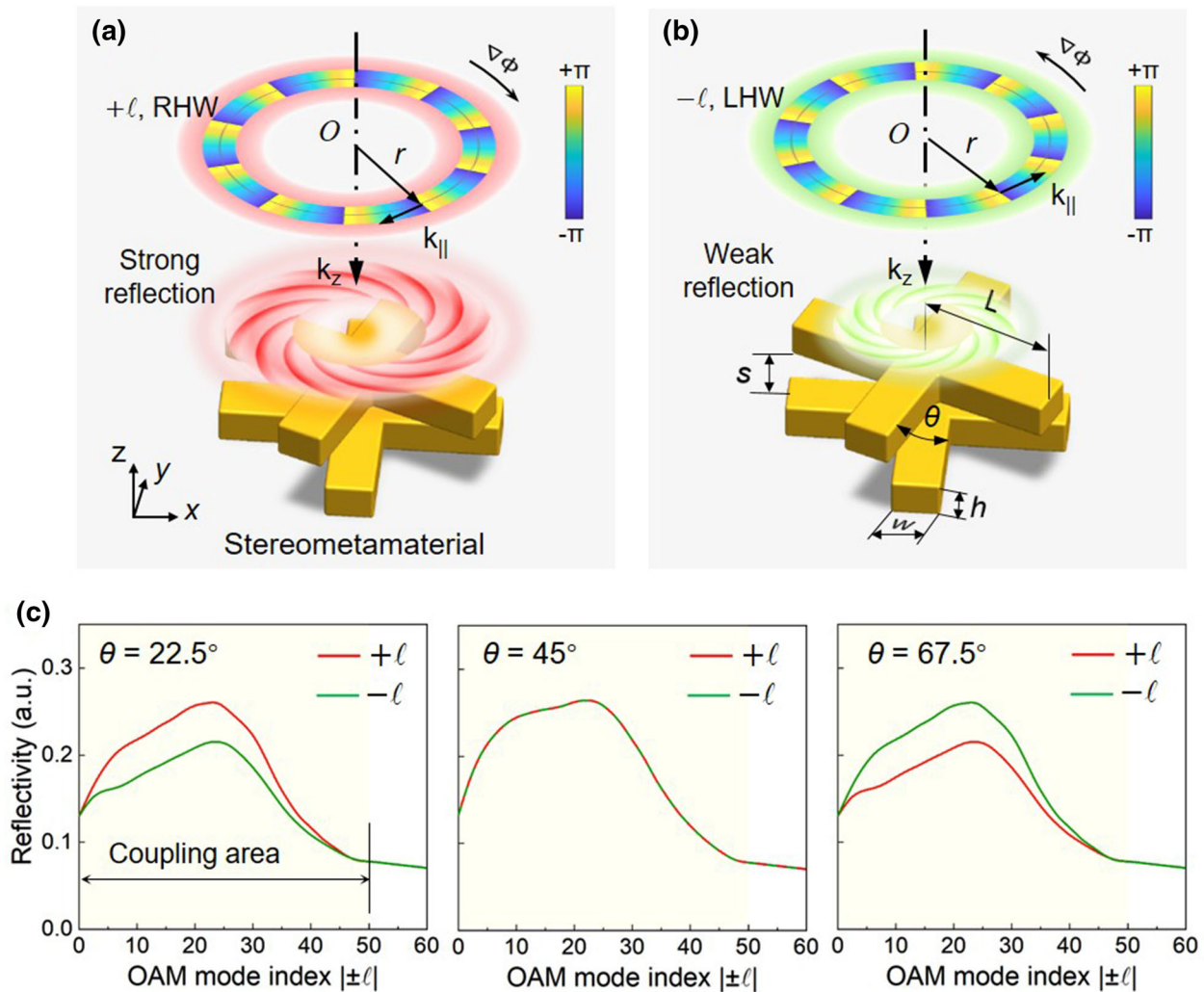
The fundamental problem is that ordinary chiral metamaterials are not suitable for the VD tailor due to their binary chiral configurations (left- or right-handed). In general, ordinary chiral metamaterials in chiroptical responses can be divided into two types: planar 2D metamaterials[36–38] and solid 3D metamaterials.[39–42] However, recent experiments have also shown that stereometamaterials, which mean quasi-3D architectures formed by achiral/chiral building blocks, can also yield

**ADVANCED
SCIENCE NEWS**

www.advancedsciencenews.com

LASER
& PHOTONICS
REVIEWS

www.lpr-journal.org

Figure 1. Concept of tailoring VD on the twisted stereometamaterials via photonic OAM. a) Incident characteristics (top) and strong reflection (middle) of optical vortices with positive/RHW OAM modes on the twisted stereometamaterial (bottom). RHW: right-handed helical wavefront. b) Corresponding to negative/LHW OAM modes. LHW: left-handed helical wavefront. c) Simulated reflection spectra for opposite OAM modes on the 22.5° (left), 45° (middle), and 67.5° (right) twisted stereometamaterials at an identical wavelength of 800 nm.

remarkable chiroptical responses.[43–46] Compared with solid 3D metamaterials, the stereometamaterials have lower requirements of spatial processing capabilities. Moreover, they have multiple chiral configurations achieved by the same building blocks but different spatial arrangements. As an important concept, the stereometamaterials have already been utilized to tailor the optical responses,[16,47] which also provide a possible solution for the OAM-dependent VD tailor.

Herein, we theoretically confirm the feasibility of tailoring VD on the designed twisted stereometamaterials and reveal its origin by discrete OAM spectra. In the experiment, the fabricated twisted stereometamaterials with multiple configurations can exhibit −97–+98% tailorable VD signals at a fixed wavelength of 800 nm. In addition, the flexible VD tailor that allows full modulation of all three VD characteristics can also be realized by engineering the geometrical parameters (e.g., length L and width w) and symmetry of the twisted stereometamaterials. This OAM-dependent tailorable VD enriches the chiroptical phenomena and

can potentially facilitate the design of advanced stereo-photonic systems with anticipated OAM responses.

2. Result

2.1. Concept of Tailoring OAM-Dependent VD on the Twisted Stereometamaterials

Schematics of the OAM-dependent VD on the twisted stereometamaterial are illustrated in **Figure** 1a,b. Distinguishing from the utilization of continuous-wavelength circularly polarized light in SAM-contributed CD, the VD is dominated by photonic OAM and requires optical vortices with varying OAM modes as the excitation sources (Figure S1, Supporting Information). For the optical vortex carrying OAM, its helical wavefront originates from the phase distribution $e^{i\ell\varphi}$, where the integer ℓ is unbounded OAM mode index, φ is azimuthal angle.[48] The OAM modes of optical vortices are positive and negative for

**ADVANCED
SCIENCE NEWS**

www.advancedsciencenews.com

LASER
& PHOTONICS
REVIEWS

www.lpr-journal.org

right- (RHW) and left-handed helical wavefront (LHW), respectively. As shown in the top panels of Figure 1a,b, optical vortices with opposite OAM modes $(+\ell, -\ell)$ have opposite phase gradients $\nabla\Phi$ and pseudo-wavevector $k_\parallel$ but the same annular intensity radius r in the transmission plane.

Then, the optical vortices with tunable OAM modes $(+\ell, -\ell)$ are normally incident on the twisted stereometamaterial to excite chiroptical response. For the opposite incident OAM modes, the stereometamaterial will exhibit an OAM-dependent differential reflection effect (middle panels), which is a direct manifestation of the VD response. The geometrical parameters of the designed twisted stereometamaterials are shown in the bottom panel of Figure 1b. The twisted stereometamaterial consists of two stacked achiral crosses, which have the same length L, width w, and height h. The two crosses are twisted to each other at an angle of θ and separated by a distance of s. Considering the radii of incident optical vortices, the structural parameters of stereometamaterials are $L = 8$ μm, $s = 0$ μm and $w = h = 3$ μm for effective light-matter coupling in our experiments. Notably, the twisted stereometamaterial has a typical fourfold rotational symmetry (C_4) with respect to the central axis and its spatial configuration is determined by the twisted angle θ.

The core of tailoring VD is controlling the reflection difference of the opposite optical vortices $(+\ell, -\ell)$, in which the configuration of the twisted stereometamaterial plays a crucial role. Specifically, the VD response behavior of the stereometamaterial can be substantially modified by altering the twisted angle θ. In order to confirm this conjecture, numerical simulations are performed based on the commercial finite-difference time-domain (FDTD) algorithm (Section 4). To avoid the chiral interference of photonic SAM, the incident optical vortices are adjusted to the linear polarization state along the x-direction. By scanning the OAM mode from -60 to $+60$, the reflection spectra on various stereometamaterials can be obtained at an operating wavelength of 800 nm. Figure 1c shows the simulated reflection spectra of 22.5° (left), 45° (middle), and 67.5° (right) stereometamaterials, respectively. For the left-handed configuration of 22.5°, the reflectivity of the optical vortex with a positive index $(+\ell)$ is always greater than that with a negative one $(-\ell)$ in the coupling area $(|\pm\ell| < 50)$, implying the occurrence of VD. For an achiral 45° stereometamaterial, it shows the same reflectivity for the opposite OAM modes in the entire scanning range. Compared with the 22.5° stereometamaterial, 67.5° stereometamaterial exhibits inverse reflection spectra. In contrast to the giant VD signals, the SAM-dependent CD responses on the stereometamaterials are extremely weak (Figures S2 and S3, Supporting Information). Besides, the VD does not depend on the wavelength and can be induced in a broadband range (Figure S4, Supporting Information). Generally, tailoring VD can be easily realized by altering the twisted angle θ, which lays the theoretical foundation for the subsequent experiments.

2.2. Origin of the VD Phenomena on the Stereometamaterials

In order to reveal the differential transmission mechanism of the opposite OAM modes on the stereometamaterial, the process of light-matter interaction need to be analyzed. Without loss of generality, we study the interaction between $\ell = \pm10$ modes and 22.5° stereometamaterial. A single-layer cross metamaterial

is used as a control in our experiment. At the beginning, the original optical vortices with opposite OAM modes have mirror-image symmetric electric field distributions. After interacting with the metamaterial, the electric field distributions of optical vortices are modulated. For the single-layer metamaterial, we focus our attention on its central plane P_1 along z axis (**Figure** 2a). The electric field distributions $|E_x|$ in the P_1 plane are monitored and recorded, as demonstrated in Figure 2b. Owing to the achiral geometrical features of the single-layer metamaterial, the electric field distributions of $|E_x^{+10}|$ and $|E_x^{-10}|$ are still symmetrical, implying that their total optical intensity is equal. In comparison, Figure 2d shows the schematic of a 22.5° stereometamaterial illuminated by the opposite optical vortices. For the 22.5° twisted stereometamaterial, we are interested in the central plane P_2 of its lower layer. In the P_2 plane, the electric field distributions are asymmetrically modified by the coupling-modulation of two layers as well as the mirror symmetry of $|E_x^{+10}|$ and $|E_x^{-10}|$ is broken (Figure 2e). Obviously, the transmissive electric field intensity of $\ell = -10$ is stronger than that of $\ell = +10$ in the P_2 plane, which is an intuitive display of the VD phenomenon. Compared with the twisted stereometamaterials, the VD signals cannot be induced by the twisted planar metamaterials (Figure S5, Supporting Information).
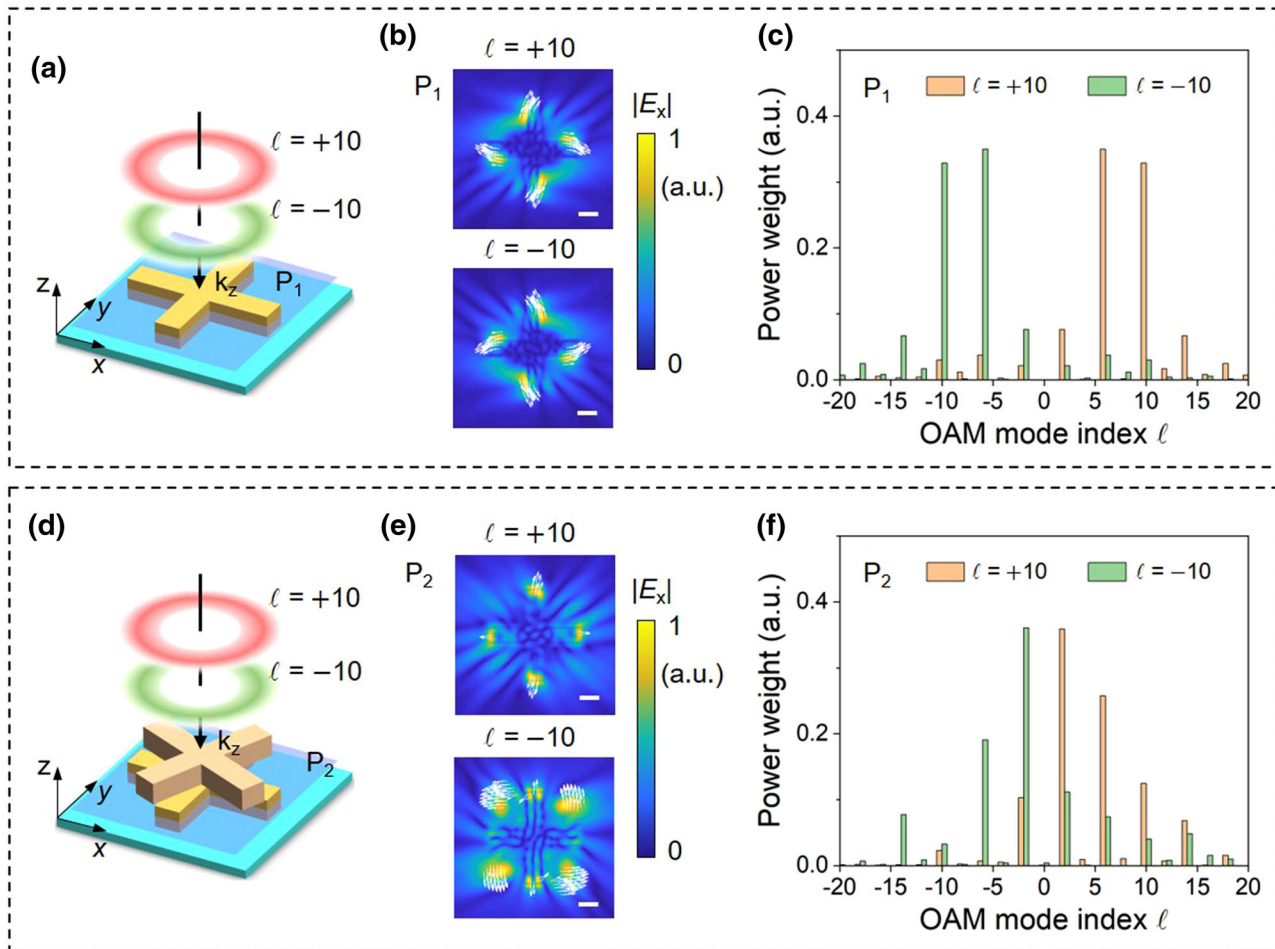
The origin of VD phenomenon can also be explained by the OAM mode conversion of incident optical vortex. Generally, the azimuthal angular electric field distribution $E(\rho, \varphi)$ can be regarded as the composition of countless orthogonal basis with ratio $\psi_\ell(\rho)$ in the Hilbert space, where ρ is the distance from the center phase singularity, and φ is the azimuth angle. Therefore, the corresponding OAM spectrum $\psi_\ell(\rho)$ can be described as

$$\psi_\ell(\rho) = \frac{1}{\sqrt{2\pi}}\int_{-\pi}^{+\pi} E(\rho, \varphi)e^{-i\ell\varphi}d\varphi \tag{1}$$

The simulated discrete OAM spectra of opposite optical vortices at planes P_1 and P_2 are shown in Figure 2c,f, respectively. Interestingly, some power weights appear at the new OAM modes resulting from the OAM-mode conversion. In the P_1 plane of the single-layer metamaterial, the OAM spectra of the opposite incident modes $(\ell = \pm10)$ are symmetrical with respect to $\ell = 0$ and still maintain high power weights at the original indices. Different from the case of P_1 plane, the power weights decrease dramatically at the position of $\ell = \pm10$ in the P_2 plane, owing to the strong electric field modulation by the twisted stereometamaterial. Besides, the OAM spectra are asymmetrical due to the different modulation levels for the opposite OAM modes. From this perspective, the origin of VD can be seen as the symmetric breaking of discrete OAM spectra.

2.3. Reflection Spectra and VD Characterizations of Varying Stereometamaterials

In the experiment, the stereometamaterials were prepared in SZ2080 photoresist by the direct-laser-writing technique (Experimental section). To yield a strong OAM coupling, all of the fabricated stereometamaterials have the same size of $L = 8$ μm, $s = 0$ μm and $w = h = 3$ μm, which are consistent with the parameters in the simulation. The twisted angle θ is set from 0° to 90° at

ADVANCED
SCIENCE NEWS
www.advancedsciencenews.com

LASER
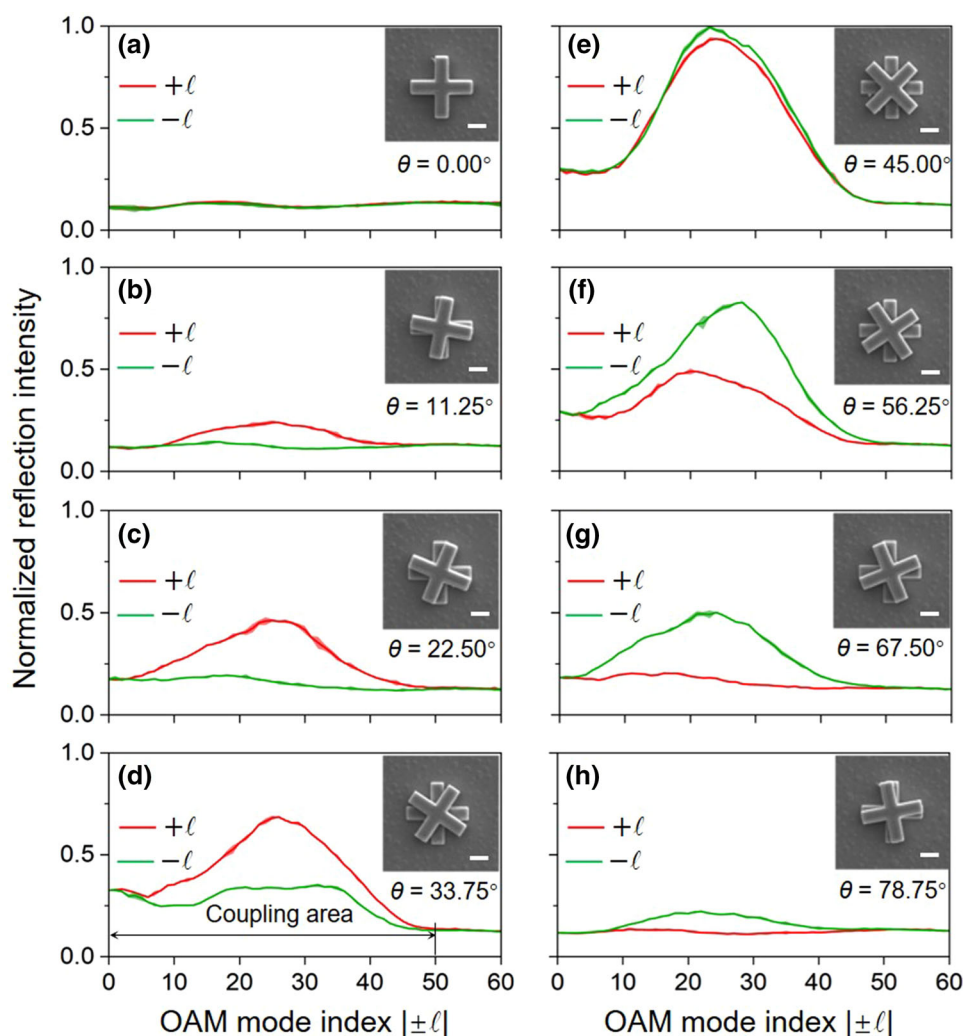& PHOTONICS
REVIEWS

www.lpr-journal.org

Figure 2. Origin of the VD phenomena on the twisted stereometamaterials. a) A single-layer metamaterial excited by the optical vortices with opposite OAM modes ($|\ell| = \pm 10$). The monitoring plane P_1 is located at the center of the metamaterial. b) Symmetric electric field distributions of $\ell = +10$ (top) and $\ell = -10$ (bottom) in the P_1 plane. White arrows indicate the Poynting vectors. c) Symmetrical discrete OAM spectra in the P_1 plane. d) Bilayer stereometamaterial with a twisted angle of 22.5°. The monitoring plane P_2 is located at the center of its lower layer. e) Symmetry-broken electric field distributions for opposite OAM modes in the P_2 plane. f) Asymmetric discrete OAM spectra in the P_2 plane. Scale bars, 4 μm.

intervals of 11.25° for generating varying spatial configurations. The range of the OAM mode index adopted in the experiment is from −60 to +60, which can completely cover the theoretical VD coupling area. By the designed measurement apparatus, the beams with varying OAM modes can be generated (Figure S6, Supporting Information). From the Debye vector diffraction theory (Experimental section), the light transmission of optical vortices with different polarization states and OAM modes under a high NA objective lens can be accurately predicted (Figures S7 and S8, Supporting Information). In our measurement, the reflection spectra of various stereometamaterials are monitored at $\lambda = 800$ nm, as shown in **Figure 3**.

In terms of all configurations, the best coupling conditions can be obtained at the OAM modes of $|\pm\ell| = 28$. When the annular radius r of the optical vortex is larger than the arm length L of the stereometamaterials ($|\pm\ell| > 50$), the reflection intensity of opposite OAM modes is equal, resulting in a near-zero VD signal. Besides, due to the C_4 feature of the twisted stereometamaterials, the normalized reflectivity (R) has spatial inversion symmetry, which can be summarized as $R_\theta^{\pm\ell} = R_{90°-\theta}^{\mp\ell}$. For the two special

achiral configurations of $\theta = 0°$ and $\theta = 45°$, the reflection intensity of opposite OAM modes is almost the same, as shown in Figure 3a,e. The slight difference may be caused by manufacturing errors. Compared with 0° stereometamaterial, the reflection enhancement of the 45° stereometamaterial is due to the less transmission caused by the expansion of contact interface. In general, in the left-handed interval of $\theta \in (0°, 45°)$, the reflection intensity of positive OAM mode is always greater than that of negative one. Moreover, the difference between the two modes undergoes a process of "no difference (0°), increased difference (11.25°), maximum difference (22.5°), decreased difference (33.75°), no difference (45°) (Figure 3a–e)". However, the relationship is reversed in the right-handed interval of $\theta \in (45°, 90°)$ (Figure 3e–h). Therefore, it can be considered that there are four special configurations: two achiral configurations of 0° and 45°, an ultra-left-handed configuration of $\theta = 22.5°$, an ultra-right-handed configuration of $\theta = 67.5°$. Besides, for the two stereometamaterials with complementary angles to each other, they appear inverse reflection intensity for opposite OAM modes. The reflection spectra of the stereometamaterials excited by circularly polarized optical

**ADVANCED
SCIENCE NEWS**

www.advancedsciencenews.com

LASER
& PHOTONICS
REVIEWS

www.lpr-journal.org

Figure 3. Experimental reflection spectra of varying stereometamaterials with twisted angles from 0° to 78.75°. a,e) Two achiral configurations with twisted angles of a) 0° and e) 45°, respectively. b–d) Three left-handed configurations with twisted angles of b) 11.25°, c) 22.5°, and d) 33.75° (d), respectively. f–h) Three right-handed configurations with twisted angles of f) 56.25°, g) 67.5°, and h) 78.75°, respectively. Solid lines represent the mean value and the shading indicates the standard deviation of multiple measurements. Insets are scanning electron microscope (SEM) images of the fabricated stereometamaterials at the corresponding twisted angles. Scale bars, 4 μm.

vortices are also observed, which shows the irrelevance of VD and photonic SAM (Figure S9, Supporting Information).

In order to visually evaluate the OAM-dependent chiroptical response, the VD at twisted angle θ is defined as

$$\text{VD}_{|\ell|} = \frac{R_\theta^{+\ell} - R_\theta^{-\ell}}{\left(R_\theta^{+\ell} + R_\theta^{-\ell} \right)/2} \times 100\% \tag{2}$$

where R represents the reflection intensity, and its superscript is the OAM mode index. It is worth noting that the effective value range of the VD is [−200%, +200%] according to the Equation (2). **Figure** 4a shows experimental VD spectra of the twisted stereometamaterials with selected configurations in Figure 4b. At the achiral beginning of $\theta = 0°$, the VD spectrum always remains approximately 0. As θ increases from 0° to 90°, the stereometamaterial firstly enters the left-handed (LH) area, then enters the right-

handed (RH) area after passing through another achiral state of $\theta = 45°$. In the left-handed area, the VD signals are always positive and reach to the maximum at the ultra-left-handed conformation of $\theta = 22.5°$. Correspondingly, in the right-handed area, the VD signals are always negative and reach to the minimum at the ultra-right-handed configuration of $\theta = 67.5°$. The spectra of two additional angles (39.375° and 50.625°) are aimed to confirm the stability of this trend.

For all of the experimental VD spectra, there are conspicuous global coupling peaks at almost the same position of $|\ell| = 28$. In Figure 4c, the peak magnitudes are replotted as a function of θ (the black dots). Obviously, it is a sinusoidal-like curve of $\gamma = A \sin(4\theta)$, where A is 94% by the numerical fitting. The experimental results are highly consistent with the fitting results. Overall, the twisted stereometamaterials with multiple configurations can exhibit a wide range of tailorable VD (−97–+98%) at the visible wavelength, which means that the sign and
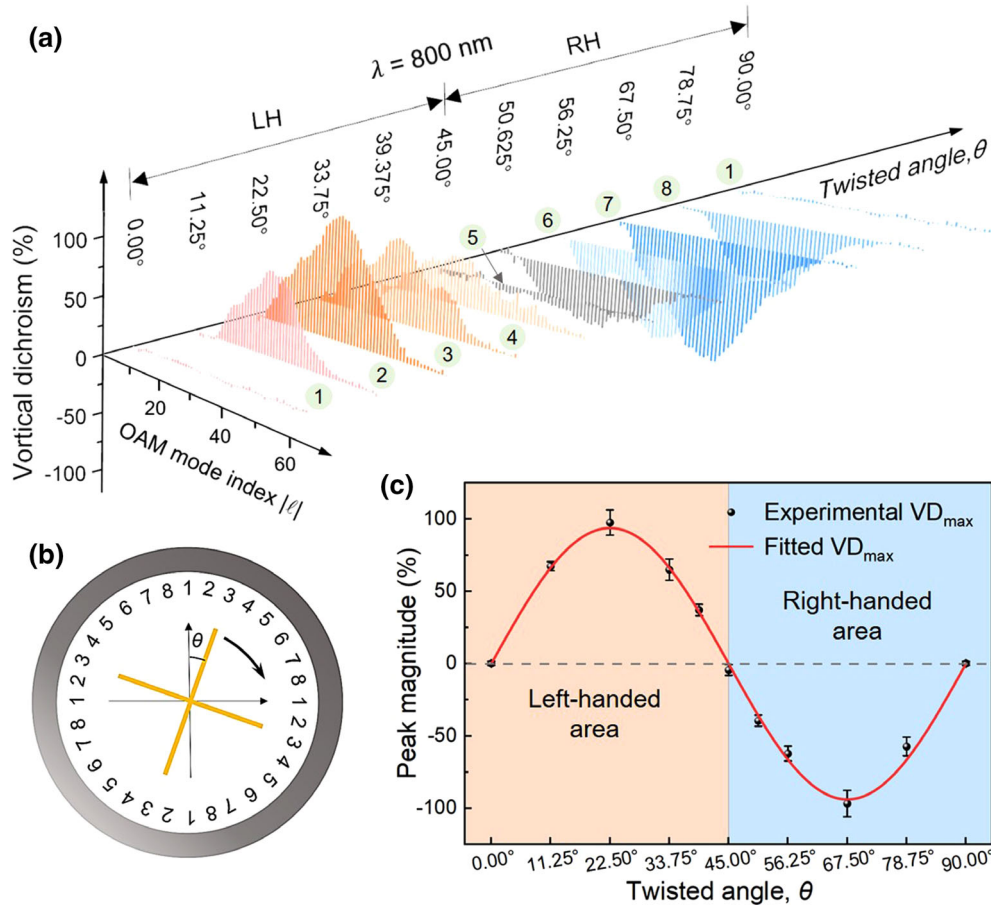
Figure 4. Characterization of vortical dichroism spectra of the stereometamaterials. a) VD spectra of various stereometamaterials at the fixed wavelength of 800 nm. b) Schematic of selected twisted angles during clockwise rotation. c) The peak magnitudes of VD (black dots) and fitted results (red line) as a function of twisted angle θ, indicting the sign and magnitude tailor in the VD spectra. The experimental data is fitted by the sine function of $y = 94\% \sin(4\theta)$.
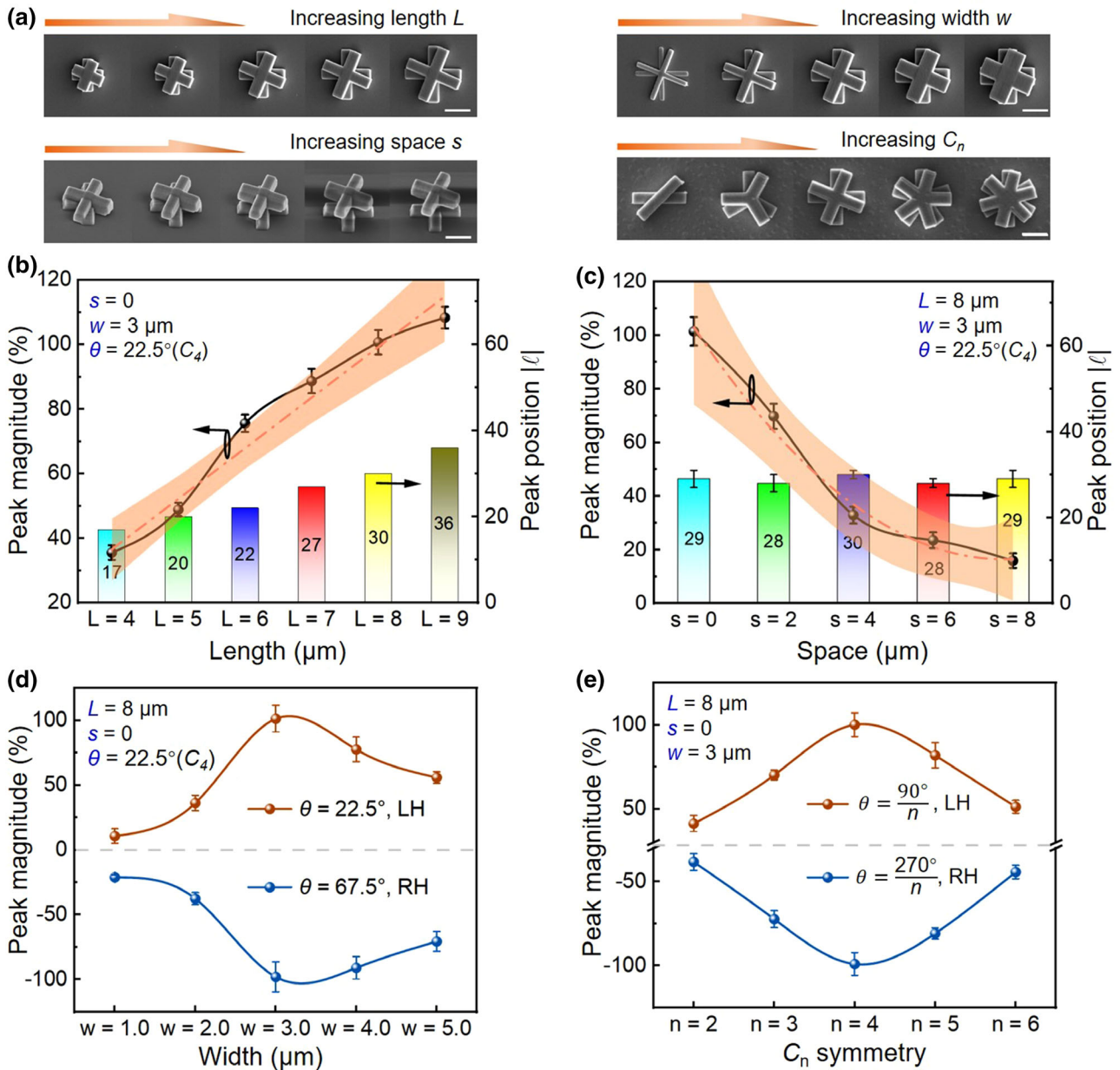
magnitude tailor in the VD characteristics can be realized at the same time. The configuration information of the stereometamaterial can be transformed into a VD spectrum, and the correlation model of twisted angle θ and coupling peak is established. Compared with stereometamaterials, the twisted planar metamaterials have the same reflection modulation for the opposite OAM modes (Figures S10 and S11, Supporting Information). As such, this VD tailor reveals a novel mechanism and has an essential difference with CD, which can be regarded as a complement of the chiroptical phenomenon in the photonic OAM dimensions.

2.4. Parameter-Tailored Relationships on the Stereometamaterials

In addition to the twisted angle θ, other geometrical parameters (including arm length L, layer space s, arm width w, and rotational symmetry C_n) of the stereometamaterial will also have impacts on the VD. To intuitively clarify the dependence of VD on a specific parameter, parameter-tailored experiments are performed. Specifically, we observe the changes of VD peaks by indepen-

dently tuning one parameter while keeping others unchanged, as shown in **Figure** 5a. By this univariate control method, the complexity of numerous parameters can be reduced. Notably, we define the peak position as the abscissa of the coupling peak in the VD spectrum, and the peak magnitude as its ordinate.

Firstly, by increasing the arm length L from 3 to 9 μm, the peak magnitude increases approximately linearly from 35% to 108% (left axis), and the peak position gradually shifts to a larger OAM index from $|\ell| = 17$ to $|\ell| = 36$ (right axis), as shown in Figure 5b. The results indicate that the increase of L will shift the peak position to the right (Figure S12, Supporting Information). It is worth noting that L is the predominate parameter that can affect the VD characteristic of peak position. Then, we focus on the impact of layer space s on VD characteristic, as shown in Figure 5c. By adding an achiral micropillar as a support between the two layers of the stereometamaterial, the layer space can be flexibly controlled without obviously affecting the measurement results (Figure S13, Supporting Information). As s increases from 0 to 8 μm, the magnitude of coupling peak drops from 100% to 16% because of the reduced interlayer coupling with an increased s. Meanwhile, the peak position has not changed significantly.

ADVANCED
SCIENCE NEWS

www.advancedsciencenews.com

LASER
& PHOTONICS
REVIEWS

www.lpr-journal.org

Figure 5. Parameter-tailored relationships on the stereometamaterials. a) SEM images of the twisted stereometamaterials with varying structural parameters, including arm length L, space s, width w, and rotational symmetry C_n. Scale bars, 5 μm. b,c) The magnitude (left axis) and position (right axis) of VD peaks as functions of b) length L and c) space s, respectively. d,e) The magnitude of VD peaks as functions of d) width w and e) rotational symmetry C_n, respectively. LH/RH: left-/right-handed stereometamaterials.

In terms of width w, the peak magnitude first increases and then decreases as w increases from 1.0 to 5.0 μm, where its maximum can be achieved at $w = 3.0$ μm (Figure 5d). Similarly, Figure 5e shows an analogous trend to w when tuning the rotational symmetry C_n of the stereometamaterials. For the stereometamaterials with different C_n symmetries, we all select the ultra-left-handed ($\theta = 90°/n$) and ultra-right-handed ($\theta = 270°/n$) configurations for generality. Obviously, the maximum magnitude of VD can be gained at C_4 symmetry in our experiments. From the SEM images in Figure 5a, we can find both w and C_n determine the contact area in the light-matter interaction. In the experiment, the stereometamaterial has an optimal contact area for coupling the photonic OAM. If the w/C_n is too large or too small, it will cause a poor coupling state. As such, w and C_n have a similar effect on the VD tailor. Therefore, varying VD tailor trends can be flexibly obtained through the adjustment of specific parameters (Figure S14, Supporting Information), which enables the stereometamaterial a potential platform for the manipulation of OAM beam. Besides, the excitation energy has little effect on the VD spectra (Figure S15, Supporting Information), indicating that a strong OAM-matter interaction can be obtained with broad power tolerance.

3. Conclusion

In summary, we have theoretically and experimentally demonstrated the concept of tailoring VD on the twisted stereometamaterials via photonic OAM. Using the fabricated twisted stereometamaterials with C_4 symmetry, a tailorable VD signal ranging from −97% to +98% can be obtained at a fixed wavelength of 800 nm. Moreover, by independently tuning the specific parameters and symmetric features of the stereometamaterials, diverse VD responses can be obtained, which enabled us to control all three VD characteristics (sign, magnitude, and position). This work opens a new dimension of photonic angular momentum in chiral optics and provides an innovative perspective for next-generation chiroptical spectroscopy. In particular, we expect that the flexible VD tailor can advance the manipulation of OAM beams and the design of miniaturized stereo-photonic devices.

4. Experimental Section

Numerical Simulation: The reflection numerical simulations were performed by the software of Lumerical FDTD Solutions. In the simulation, the refractive index of the twisted stereometamaterial was set to be 1.51. Perfectly matched layer boundaries were applied for the X, Y, and Z directions, and the minimum mesh step was set to be 50 nm. The incident electrical field distribution in polar coordinate space ($E^{in}(r, \varphi)$) of linearly polarized optical vortex can be described as

$$E^{in}(r, \varphi) = C \frac{r^{|\ell|}}{\sqrt{|\ell|!}} \exp\left(-\frac{r^2}{w_0^2}\right) \exp(i\ell\varphi) \, \hat{x} \qquad (3)$$

where C is a normalized constant independent of ℓ and r, w_0 is the beam waist corresponding to experimental conditions, which is equal to 2 μm. The wavelength of the light source is fixed at 800 nm. In the reflection spectrum, the weak absorption of light by the photoresist material can be ignored, so the reflectance R is equal to the difference between 1 and the transmittance T.

Twisted Stereometamaterials Preparation and Characterization: The twisted stereometamaterials used in the experiment were manufactured by the direct laser writing (DLW) process. We use a commercial zirconium-silicon hybrid sol-gel material (SZ2080, IESL-FORTH, Greece) for the photopolymerization. After pre-baking process at 100 °C for 30 min to evaporate the solvent in the material, the designed stereometamaterials can be polymerized inside the material by the DLW. Then the sample was developed in absolute ethanol for 30 min until the unpolymerized portion was completely dissolved. The scanning electron microscopy (SEM) images were achieved by a secondary-electron scanning electron microscope (EVO18, ZEISS) with an accelerating voltage of 10 keV after depositing ≈10 nm of gold.

Focused Light Field Analysis: At the entrance pupil (r_1, φ_1, z_1) of the objective lens, the diffracted electric field can be derived from Fresnel diffraction theory as

$$E_1^{in}(r_1, \varphi_1, z_1) = -\frac{\exp(ikz_1)}{i\lambda z_1} \exp\left(\frac{ikr_1^2}{2z_1}\right) \int_0^R \int_0^{2\pi} P(r, \varphi)$$

$$\times \exp\left(\frac{ikr^2}{2z_1}\right) \exp\left[\frac{-ikrr_1\cos(\varphi_1 - \varphi)}{z_1}\right] 2\pi r \, dr \, d\varphi \qquad (4)$$

where $P(r, \varphi) = e^{i\ell\varphi}$ is the phase of the optical vortex from SLM, λ is the wavelength of the incident light, $k = \frac{2\pi}{\lambda}$ is wavenumber. According to vectoral diffraction theory, the tightly focused electric field vector $\vec{E}_2(r_2, \varphi_2, z_2)$ in the cylindrical coordinate system can be calculated from the generalized Debye integral as

$$\vec{E}_2(r_2, \varphi_2, z_2)$$

$$= \begin{bmatrix} E_x \cdot \hat{x} \\ E_y \cdot \hat{y} \\ E_z \cdot \hat{z} \end{bmatrix} = iC \, [\hat{x}\hat{y}\hat{z}] \int_0^\Theta \int_0^{2\pi} \sin\theta \, E_1^{in}(r_1, \varphi_1, z_1) \sqrt{\cos\theta}$$

$$\cdot \begin{bmatrix} 1 + (\cos\theta - 1)\cos^2\varphi & (\cos\varphi - 1)\cos\varphi\sin\varphi & -\sin\theta\cos\varphi \\ (\cos\theta - 1)\cos\varphi\sin\varphi & 1 + (\cos\theta - 1)\sin^2\varphi & -\sin\theta\sin\varphi \\ \sin\theta\cos\varphi & \sin\theta\sin\varphi & \cos\theta \end{bmatrix}$$

$$\cdot \begin{bmatrix} p_x \\ p_y \\ p_z \end{bmatrix} \cdot \exp\{ik[z_2\cos\theta + r_2\sin\theta\cos(\varphi - \varphi_2)]\} \, d\theta d\varphi \qquad (5)$$

where C is a normalized constant, $\hat{x}$, $\hat{y}$, $\hat{z}$ are the unit vectors along the x, y, z directions, $\Theta = \sin^{-1}(\frac{NA}{n})$ is the maximum focusing angle of the objective lens, $[p_x, p_y, p_z]^T$ is a unit vector matrix about the polarization of input light. For the linearly polarized light in the x direction used in the experiment, the polarization matrix is $[1, 0, 0]^T$. For the left-handed circularly polarized light the polarization matrix is $[1, i, 0]^T$.

Supporting Information

Supporting Information is available from the Wiley Online Library or from the author.

Conflict of Interest

The authors declare no conflict of interest.

Author Contributions

S.L. and J.N. contributed equally to this work. S. L., J.N., and D.W. proposed the idea and conceived the experiment. S.L., C.Z., X.W., D.W., D.P., H.W., C.X., R.L., and J.L. performed the experiments. S.L., J.N., and G.L. performed the numerical simulations. S.L., J.N., and G.L. wrote the manuscript. J.L. and D.W. supervised the project. All authors discussed the results and commented on the manuscript.

Data Availability Statement

The data that supports the findings of this study are available in the supplementary material of this article.

[1] R. Hassey, E. J. Swain, N. I. Hammer, D. Venkataraman, M. D. Barnes, *Science* **2006**, *314*, 1437.

[2] M. S. Davis, W. Zhu, J. K. Lee, H. J. Lezec, A. Agrawal, *Sci. Adv.* **2019**, *5*, eaav8262.

[3] V. K. Valev, J. J. Baumberg, C. Sibilia, T. Verbiest, *Adv. Mater.* **2013**, *25*, 2517.

[4] J. T. Collins, C. Kuppe, D. C. Hooper, C. Sibilia, M. Centini, V. K. Valev, *Adv. Opt. Mater.* **2017**, *5*, 1700182.

[5] X. T. Kong, L. V. Besteiro, Z. Wang, A. O. Govorov, *Adv. Mater.* **2020**, *32*, 1801790.

[6] N. J. Greenfield, *Nat. Protoc.* **2006**, *1*, 2876.

[7] D. H. Kwon, P. L. Werner, D. H. Werner, *Opt. Express* **2008**, *16*, 11802.

[8] Z. Wang, F. Cheng, T. Winsor, Y. Liu, *Nanotechnology* **2016**, *27*, 412001.

[9] Y. Zhao, M. A. Belkin, A. Alu, *Nat. Commun.* **2012**, *3*, 870.

[10] E. Hendry, T. Carpy, J. Johnston, M. Popland, R. V. Mikhaylovskiy, A. J. Lapthorn, S. M. Kelly, L. D. Barron, N. Gadegaard, M. Kadodwala, *Nat. Nanotechnol.* **2010**, *5*, 783.

[11] N. A. Abdulrahman, Z. Fan, T. Tonooka, S. M. Kelly, N. Gadegaard, E. Hendry, A. O. Govorov, M. Kadodwala, *Nano Lett.* **2012**, *12*, 977.

[12] C. Chen, L. Gao, W. Gao, C. Ge, X. Du, Z. Li, Y. Yang, G. Niu, J. Tang, *Nat. Commun.* **2019**, *10*, 1927.

[13] W. Li, Z. J. Coppens, L. V. Besteiro, W. Wang, A. O. Govorov, J. Valentine, *Nat. Commun.* **2015**, *6*, 8379.

[14] A. Basiri, X. Chen, J. Bai, P. Amrollahi, J. Carpenter, Z. Holman, C. Wang, Y. Yao, *Light Sci. Appl.* **2019**, *8*, 78.

[15] A. Kuzyk, R. Schreiber, Z. Fan, G. Pardatscher, E. M. Roller, A. Hogele, F. C. Simmel, A. O. Govorov, T. Liedl, *Nature* **2012**, *483*, 311.

[16] A. Kuzyk, R. Schreiber, H. Zhang, A. O. Govorov, T. Liedl, N. Liu, *Nat. Mater.* **2014**, *13*, 862.

[17] L. Xin, C. Zhou, X. Duan, N. Liu, *Nat. Commun.* **2019**, *10*, 5394.

[18] M. Schäferling, D. Dregely, M. Hentschel, H. Giessen, *Phys. Rev. X* **2012**, *2*, 031010.

[19] K. Y. Bliokh, F. J. Rodríguez-Fortuño, F. Nori, A. V. Zayats, *Nat. Photonics* **2015**, *9*, 796.

[20] L. Allen, M. W. Beijersbergen, R. J. Spreeuw, J. P. Woerdman, *Phys. Rev. A* **1992**, *45*, 8185.

[21] M. Padgett, R. Bowman, *Nat. Photonics* **2011**, *5*, 343.

[22] D. G. Grier, *Nature* **2003**, *424*, 810.

[23] H. Ren, G. Briere, X. Fang, P. Ni, R. Sawant, S. Heron, S. Chenot, S. Vezian, B. Damilano, V. Brandli, S. A. Maier, P. Genevet, *Nat. Commun.* **2019**, *10*, 2986.

[24] X. Fang, H. Ren, M. Gu, *Nat. Photonics* **2019**, *14*, 102.

[25] H. Ren, X. Fang, J. Jang, J. Bürger, J. Rho, S. A. Maier, *Nat. Nanotechnol.* **2020**, *15*, 948.

[26] K. Toyoda, K. Miyamoto, N. Aoki, R. Morita, T. Omatsu, *Nano Lett.* **2012**, *12*, 3645.

[27] J. Ni, C. Wang, C. Zhang, Y. Hu, L. Yang, Z. Lao, B. Xu, J. Li, D. Wu, J. Chu, *Light Sci. Appl.* **2017**, *6*, e17011.

[28] A. Ambrosio, L. Marrucci, F. Borbone, A. Roviello, P. Maddalena, *Nat. Commun.* **2012**, *3*, 989.

[29] J. Wang, J.-Y. Yang, I. M. Fazal, N. Ahmed, Y. Yan, H. Huang, Y. Ren, Y. Yue, S. Dolinar, M. Tur, A. E. Willner, *Nat. Photonics* **2012**, *6*, 488.

[30] N. Bozinovic, Y. Yue, Y. Ren, M. Tur, P. Kristensen, H. Huang, A. E. Willner, S. Ramachandran, *Science* **2013**, *340*, 1545.

[31] K. A. Forbes, G. A. Jones, *Phys. Rev. A* **2021**, *103*, 053515.

[32] X. Zambrana-Puyalto, X. Vidal, G. Molina-Terriza, *Nat. Commun.* **2014**, *5*, 4922.

[33] P. Woźniak, I. De Leon, K. Höflich, G. Leuchs, P. Banzer, *Optica* **2019**, *6*, 961.

[34] W. Brullot, M. K. Vanbel, T. Swusten, T. Verbiest, *Sci. Adv.* **2016**, *2*, e1501349.

[35] J. Ni, S. Liu, D. Wu, Z. Lao, Z. Wang, K. Huang, S. Ji, J. Li, Z. Huang, Q. Xiong, Y. Hu, J. Chu, C. W. Qiu, *Proc. Natl. Acad. Sci. U. S. A.* **2021**, *118*, e2020055118.

[36] V. A. Fedotov, P. L. Mladyonov, S. L. Prosvirnin, A. V. Rogacheva, Y. Chen, N. I. Zheludev, *Phys. Rev. Lett.* **2006**, *97*, 167401.

[37] J. Ni, S. Liu, G. Hu, Y. Hu, Z. Lao, J. Li, Q. Zhang, D. Wu, S. Dong, J. Chu, C. W. Qiu, *ACS Nano* **2021**, *15*, 2893.

[38] M. Kuwata-Gonokami, N. Saito, Y. Ino, M. Kauranen, K. Jefimovs, T. Vallius, J. Turunen, Y. Svirko, *Phys. Rev. Lett.* **2005**, *95*, 227401.

[39] J. K. Gansel, M. Thiel, M. S. Rill, M. Decker, K. Bade, V. Saile, Wegener, M., *Science* **2009**, *325*, 1513.

[40] A. G. Mark, J. G. Gibbs, T. C. Lee, P. Fischer, *Nat. Mater.* **2013**, *12*, 802.

[41] C. M. Soukoulis, M. Wegener, *Nat. Photonics* **2011**, *5*, 523.

[42] J. Kaschke, M. Wegener, *Nanophotonics* **2016**, *5*, 510.

[43] M. Hentschel, M. Schäferling, X. Duan, H. Giessen, N. Liu, *Sci. Adv.* **2017**, *3*, e1602735.

[44] M. Decker, M. Ruther, C. E. Kriegler, J. Zhou, C. M. Soukoulis, S. Linden, M. Wegener, *Opt. Lett.* **2009**, *34*, 2501.

[45] M. Decker, R. Zhao, C. M. Soukoulis, S. Linden, M. Wegener, *Opt. Lett.* **2010**, *35*, 1593.

[46] H. Liu, J. X. Cao, S. N. Zhu, N. Liu, R. Ameling, H. Giessen, *Phys. Rev. B* **2010**, *81*, 241403.

[47] N. Liu, H. Liu, S. Zhu, H. Giessen, *Nat. Photonics* **2009**, *3*, 157.

[48] A. M. Yao, M. J. Padgett, *Adv. Opt. Photonics* **2011**, *3*, 161.

2100518 (9 of 9)